H_∞ Control of Nonperiodic Two-Dimensional Channel Flow

Lubomír Baramov, Owen R Tutty, and Eric Rogers

***Abstract*—This paper deals with finite-dimensional boundary control of the two-dimensional (2-D) flow between two infinite parallel planes. Surface transpiration along a few regularly spaced sections of the bottom wall is used to control the flow. Measurements from several discrete, suitably placed shear-stress sensors provide the feedback. Unlike other studies in this area, the flow is not assumed to be periodic, and spatially growing flows are considered. Using spatial discretization in the streamwise direction, frequency responses for a relevant part of the channel are obtained. A low-order model is fitted to these data and the modeling uncertainty is estimated. An H_∞ controller is designed to guarantee stability for the model set and to reduce the wall-shear stress at the channel wall. A nonlinear Navier-Stokes PDE solver was used to test the designs in the loop. The only assumption made in these simulations is that the flow is two dimensional. The results showed that, although the problem was linearized when designing the controller, the controller could significantly reduce fundamental 2-D disturbances in practice.**

***Index Terms*—H_∞-control, flow control, model validation, nonperiodic flows.**

I. Introduction

FLOW control is currently attracting considerable interest in the fluids research community. A major motivation for this is the possibility of reducing drag on a body by preventing or delaying transition from laminar to turbulent flow. The systems dealt with in these problems are, in control terms, very complex, nonlinear, and infinite dimensional, even if, in fluid mechanical terms, the structure of the flow field is simple in nature. Plane Poiseuille flow, i.e., flow between two infinite parallel plates is one of the simplest and best understood cases of fluid dynamics. Controlling this flow is, however, still an extremely challenging problem, even if it is assumed that deviations from the steady state are small enough for the governing equations to be linearized. It has become a benchmark problem for developing control algorithms for fluid flows and was considered in [4], [6], [9], [14]–[16] among others. All these references make a fundamental assumption that the flow is spatially periodic in the streamwise direction, and hence that a Fourier-Galerkin decomposition can be used to obtain independent dynamics for each respective Fourier mode. [14] proposes a simple proportional control using distributed arrays of shear sensors and thermoelectric actuators; their goal was to modify the dynamical properties of the flow by heating the fluid and changing its viscosity. A more usual way is, however, boundary control based on transpiration along one of the walls. Different strategies have been proposed, e.g., a simple integral control in [15], LQG control in [9], [16], H_∞ control in [4], [6]. [6], [15], [16] deal with the single wavenumber case: the controlled boundary condition is assumed to be harmonically distributed along the channel wall and the measurements are taken at discrete, periodically spaced points. These single wavenumber results can be extended to multiwavenumber cases using both distributed actuators and measurements, via the fast Fourier transform, [9].

An interesting result is in [2] where tangential blowing and suction was used instead of the normal one. Distributed actuation and sensing was considered and a nonlinear decentralized controller was developed. A major constraint is, however, that this method is applicable only for a limited range of Reynolds numbers.

In [4], boundary control for discrete transpiration was proposed, where blowing and suction takes place only along short, periodically spaced sections of the wall. This is a model of blowing/suction panels which are being developed and considered for use in the aerospace industry. Then, assuming point measurements, a reduced order multiwavenumber flow model was obtained. The modeling uncertainty was estimated and taken into account in the H_∞ control design.

In this paper we do not assume periodicity and consider control of a spatially developing flow. This type of flow is of considerable practical importance (see, e.g., [18]). For example, standard transition prediction methods are based on spatially growing disturbances. We shall consider mainly boundary control in the form of blowing/suction panels and discrete-points measurements, although results from a simple proportional controller based on point actuation and sensing are also presented. Specifically, we shall use four regularly spaced pairs of blowing/suction panels and five sensors—which, as will be seen below, is sufficient to reduce the wall-shear stress significantly from the actuation/sensing area downstream. Finite differences in the streamwise direction and Chebyshev polynomials across the channel are used to obtain a finite dimensional approximation of the governing equations. By a technique based on the Redheffer star product we obtain (pointwise) frequency-response data of the flow. A low-order model is then fitted on these data, and a modeling uncertainty is estimated using the frequency-domain model validation ideas of [8]. Finally, a robustly stable H_∞ controller was designed

Manuscript received January 30, 2003. Manuscript received in final form August 26, 2003. Recommended by Associate Editor A. Banaszuk. The work of L. Baramov was supported by the School of Electronics and Computer Science, University of Southampton, UK.

L. Baramov is with Honeywell Prague Laboratory, Prague, Czech Republic.

O. R. Tutty is with the School of Engineering Sciences, University of Southampton, Southampton SO17 1BJ, U.K.

E. Rogers is with School of Electronics and Computer Science, University of Southampton, Southampton SO17 1BJ, U.K.

Digital Object Identifier 10.1109/TCST.2003.821951

for this model set to reduce spatially growing components of the flow field.

A nonlinear Navier–Stokes PDE solver was used to test the designs in the loop. The only assumption made in these simulations is that the flow is two dimensional. The results reported below show that, although a linear model was used in designing it, the controller can significantly reduce fundamental two-dimensional (2-D) disturbances in practice.

Finally in this section we note that although we have specifically dropped the assumption of periodicity which is used in many other studies of flow control, including those cited above, this does not imply that a control system designed using a periodic framework will not work in a nonperiodic setting or control a spatially developing flow. The key issue here is one of localization: when using a periodic domain both the sensing and actuation need to be sufficiently compact to be independent of the size of the domain to ensure that such a control system will work in a nonperiodic setting. That this is possible has been demonstrated by Bewley [5], who has developed a method of designing controllers which satisfies this requirement based on models obtained by spatially localized convolution kernels. However, in effect these controllers require point actuation and sensing over the operating region in contrast to the control schemes developed here which require discrete actuation and sensing. The question of the degree of localization that is required is a very important question that has yet to be fully resolved. Some recent substantial results on this matter can be found in [3]. Further, as we demonstrate by an example, a simple proportional controller with point actuation and sensing can achieve a significant reduction in the size of the disturbance. Note however that this does not imply that control systems with high degree of localization are practically feasible as it may not be possible to build them. Indeed, this is a major motivation for using discrete panels as these can be constructed and applied using current technology, see, e.g., [13].

Here we are applying linear techniques to a nonlinear problem. The subject of the application of linear methods to control nonlinear perturbation of dynamic systems has been the subject of intense research effort over a long number of years and there is a very extensive literature available. The method we use here is but one of these, but clearly before meaningful comparisons between such methods can be attempted, it is necessary to extensively investigate each in turn. It is in this area that the major contributions of this paper lie.

II. Mathematical Models

A. Finite Approximations

We consider a planar flow in an infinite channel of fixed height. The flow is nondimensionalised using the channel half-height h and the center-line velocity U_0 of the undisturbed flow. We consider a coordinate system as in Fig. 1. Let $p(x,y,t)$ be the pressure and, $u(x,y,t)$ and $v(x,y,t)$ be the velocities in the direction of x and y axes, respectively. The steady base flow is given by $p(x,y,t) = -2x/\mathrm{Re}$, $u(x,y,t) = 1-y^2 =: U(y)$ and $v(x,y,t) = 0$ where $\mathrm{Re} = U_0 h/\nu$ is the Reynolds number and ν is the kinematic viscosity of the fluid. Assume that the quantities $\hat{p}(x,y,t) \equiv p(x,y,t) + 2x/\mathrm{Re}$, $\hat{u}(x,y,t) \equiv u(x,y,t) - U(y)$, and $\hat{v}(x,y,t) \equiv v(x,y,t)$ are sufficiently small for the flow to be governed by the linearized Navier-Stokes equations

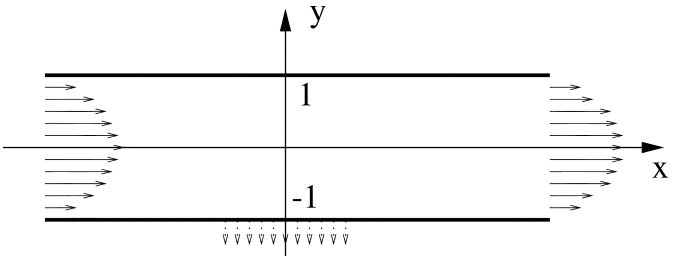

Fig. 1. Coordinate system.

$$\frac{\partial \hat{u}}{\partial t} + U\frac{\partial \hat{u}}{\partial x} + \frac{\mathrm{d}U}{\mathrm{d}y}\hat{v} = -\frac{\partial \hat{p}}{\partial x} + \frac{1}{Re}\nabla^2\hat{u} \tag{1}$$

$$\frac{\partial \hat{v}}{\partial t} + U\frac{\partial \hat{v}}{\partial x} = -\frac{\partial \hat{p}}{\partial y} + \frac{1}{Re}\nabla^2\hat{v} \tag{2}$$

$$\frac{\partial \hat{u}}{\partial x} + \frac{\partial \hat{v}}{\partial y} = 0 \tag{3}$$

where $\nabla^2 = \partial^2/\partial x^2 + \partial^2/\partial y^2$. The boundary conditions are $\hat{u}(x,1,t) = \hat{v}(x,1,t) = 0$, $\hat{u}(x,-1,t) = 0$ and $\hat{v}(x,-1,t) = -q(t)(dl(x)/dx)$. The last condition describes the wall-normal blowing/suction. The function $l(x)$ represents the geometric configuration of the blowing and suction elements. The function $q(t)$ modifies the blowing/suction according to the control law-it is the normalized suction velocity through the wall. In the case of several independent actuators we may consider q to be an m-dimensional row vector and l an m-dimensional column vector.

To write the Navier-Stokes equations into the form used in this study, we use the so-called modified stream function Φ as in [15], [16], i.e., let

$$\hat{u}(x,y,t) = \frac{\partial \Phi(x,y,t)}{\partial y} + l(x)q(t)\frac{\partial f(y)}{\partial y} \tag{4}$$

$$\hat{v}(x,y,t) = -\frac{\partial \Phi(x,y,t)}{\partial x} - \frac{\partial l(x)}{\partial x}q(t)f(y) \tag{5}$$

where $f(y)$ is any smooth function which satisfies $f(-1) = 1$ and $f(1) = (\partial f(y)/\partial y)|_{y=-1,1} = 0$. Equations (1)–(3) now become

$$\begin{aligned}\frac{\partial}{\partial t}\nabla^2\Phi = &-U\frac{\partial}{\partial x}\nabla^2\Phi + \frac{d^2U}{dy^2}\frac{\partial \Phi}{\partial x} + \frac{1}{\mathrm{Re}}\nabla^4\Phi - \dot{q}\nabla(fl)\\ &- q\left[U\frac{\partial}{\partial x}\nabla^2(fl) - \frac{d^2U}{dy^2}f\frac{dl}{dx} - \frac{1}{Re}\nabla^4(fl)\right]\end{aligned} \tag{6}$$

with boundary conditions $\Phi = \partial\Phi/\partial y = 0$ for $y = \pm 1$. As an output we use the streamwise shear stress component at a point x_n on the lower wall given by

$$z_n = \left(\frac{\partial^2\Phi}{\partial y^2} + q\frac{\partial^2 f}{\partial y^2}l\right)\Big|_{y=-1, x=x_n}. \tag{7}$$

The surface shear stress is used as the output as this is one of the quantities that it would be feasible to measure in an experiment.

To obtain a finite-dimensional approximation of the above system of equations we use, as in [4], [15], [16], a Chebyshev expansion in the cross channel direction. We use a finite-difference scheme in the streamwise direction. Assume that the x-coordinate is discretized into regularly spaced samples $\{x_n, n = \ldots, -1, 0, 1, \ldots\}$, where $x_n = x_{n-1} + \delta$ where δ is a constant. The function Φ is now represented at these discrete points for $n = \ldots, -1, 0, 1, \ldots$ as

$$\Phi(x_n, y, t) \approx \sum_{m=0}^{M+4} \xi_{nm}(t)\Gamma_m(y) \tag{8}$$

where $\Gamma_m(y)$ are Chebyshev polynomials. The boundary conditions are satisfied by requiring that for $n = \ldots, -1, 0, 1, \ldots$

$$\sum_{m=0}^{M+4} \xi_{nm} \left[\Gamma_m, \frac{\partial \Gamma_m}{\partial y}\right]_{y=\pm 1} = \mathbf{0}. \tag{9}$$

Using (9) the functions $\xi_{nM+1}, \ldots, \xi_{nM+4}$ can be expressed in terms of $\xi_{n0}, \ldots, \xi_{nM}$.

The partial derivatives $\partial^k/\partial x^k$ $k = 1, \ldots, 4$ are approximated by symmetric difference formula as

$$\begin{aligned}
\left\{\frac{\partial \Phi}{\partial x}\right\}_{x=x_i} &= \frac{\Phi_{i+1} - \Phi_{i-1}}{2\delta} \\
\left\{\frac{\partial^2 \Phi}{\partial x^2}\right\}_{x=x_i} &= \frac{\Phi_{i+1} - 2\Phi_i + \Phi_{i-1}}{\delta^2} \\
\left\{\frac{\partial^3 \Phi}{\partial x^3}\right\}_{x=x_i} &= \frac{\Phi_{i+2} - 2\Phi_{i+1} + 2\Phi_{i-1} - \Phi_{i-2}}{2\delta^3} \\
\left\{\frac{\partial^4 \Phi}{\partial x^4}\right\}_{x=x_i} &= \frac{\Phi_{i+2} - 4\Phi_{i-1} + 6\Phi_i - 4\Phi_{i-1} + \Phi_{i-2}}{\delta^4}
\end{aligned} \tag{10}$$

where $\Phi_i = \Phi(x_i, y, t)$. Once the problem has been discretised spatially using ((6)–(10)), a standard Galerkin procedure (see [7] or [15]) is now used to produce for the n-th grid point a set of $2(M+1)$ ordinary first-order equations which can be written as

$$\begin{aligned}
\dot{\boldsymbol{x}}_{\boldsymbol{n}} = {} & \boldsymbol{A}\boldsymbol{x}_{\boldsymbol{n}} + \boldsymbol{B}_{\boldsymbol{1n}} q + \boldsymbol{B}_{\boldsymbol{2n}} \dot{q} + \boldsymbol{B}_{\boldsymbol{-2}} \boldsymbol{x}_{\boldsymbol{n-2}} \\
& + \boldsymbol{B}_{\boldsymbol{-1}} \boldsymbol{x}_{\boldsymbol{n-1}} + \hat{\boldsymbol{B}}_{\boldsymbol{-1}} \dot{\boldsymbol{x}}_{\boldsymbol{n-1}} \\
& + \boldsymbol{B}_{\boldsymbol{+1}} \boldsymbol{x}_{\boldsymbol{n+1}} + \hat{\boldsymbol{B}}_{\boldsymbol{+1}} \dot{\boldsymbol{x}}_{\boldsymbol{n+1}} + \boldsymbol{B}_{\boldsymbol{+2}} \boldsymbol{x}_{\boldsymbol{n+2}}
\end{aligned} \tag{11}$$

where $\boldsymbol{x_n} = [\xi_{n0} \quad \cdots \quad \xi_{nM}]^T$. Notice that the matrices above are the same for all grid points, except for $\boldsymbol{B_{1n}}$ and $\boldsymbol{B_{2n}}$ which express the effect of the boundary input and depend on $l(x_{n-2}), \ldots, l(x_{n+2})$. Note also that due to the properties of Chebyshev polynomials, the above equation can be split into two independent ones, solving for ξ_{nm} with m either even or odd. The details are omitted here for brevity.

The output approximating shear at the nth gridpoint becomes

$$z_n = \sum_{n=-N}^{N} \boldsymbol{C}\boldsymbol{x_n} + D_n q. \tag{12}$$

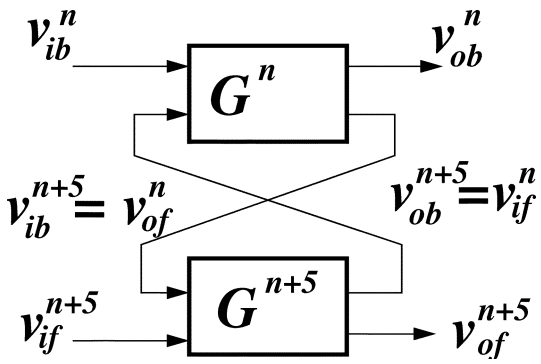

Fig. 2. Star product.

To condense the notation, we combine the equations for a set of 5 grid points as

$$\dot{\boldsymbol{x}}_{\boldsymbol{sn}} = \boldsymbol{A}_{\boldsymbol{s}} \boldsymbol{x}_{\boldsymbol{sn}} + \boldsymbol{B}_{\boldsymbol{1n}} \boldsymbol{v}_{\boldsymbol{ib}}^{\boldsymbol{n}} + \boldsymbol{B}_{\boldsymbol{2}} \boldsymbol{v}_{\boldsymbol{if}}^{\boldsymbol{n}} \tag{13}$$

where

$$\boldsymbol{x}_{\boldsymbol{sn}} = \begin{bmatrix} \boldsymbol{x_n} \\ \vdots \\ \boldsymbol{x_{n+4}} \end{bmatrix}, \quad \boldsymbol{v}_{\boldsymbol{ib}}^{\boldsymbol{n}} = \begin{bmatrix} \boldsymbol{x_{n-2}} \\ \boldsymbol{x_{n-1}} \\ \dot{\boldsymbol{x}}_{\boldsymbol{n-1}} \\ q \\ \dot{q} \end{bmatrix} \tag{14}$$

$$\boldsymbol{v}_{\boldsymbol{if}}^{\boldsymbol{n}} = \begin{bmatrix} \boldsymbol{x_{n+6}} \\ \boldsymbol{x_{n+5}} \\ \dot{\boldsymbol{x}}_{\boldsymbol{n+5}} \end{bmatrix}. \tag{15}$$

Here the sub-script ib and if stand for input-back and input-forward, respectively. The outputs which are fed-back and fed-forward from this system are denoted by

$$\boldsymbol{v}_{\boldsymbol{ob}}^{\boldsymbol{n}} = \begin{bmatrix} \boldsymbol{x_{n+1}} \\ \boldsymbol{x_n} \\ \dot{\boldsymbol{x}}_{\boldsymbol{n}} \end{bmatrix}, \quad \boldsymbol{v}_{\boldsymbol{of}}^{\boldsymbol{n}} = \begin{bmatrix} \boldsymbol{x_{n+3}} \\ \boldsymbol{x_{n+4}} \\ \dot{\boldsymbol{x}}_{\boldsymbol{n+4}} \\ q \\ \dot{q} \end{bmatrix}. \tag{16}$$

We can conveniently form the transfer function matrix $\boldsymbol{G^n}(s)$ mapping Laplace transform images of $\boldsymbol{v_{ib}^n}$, $\boldsymbol{v_{if}^n}$ to the Laplace images of $\boldsymbol{v_{ob}^n}$, $\boldsymbol{v_{of}^n}$. To get a model of two adjacent segments with a total 10 grid-points, we need a feedback interconnection of $\boldsymbol{G^n}(s)$ and $\boldsymbol{G^{n+5}}(s)$ as in Fig. 2, known in the robust control literature (e.g., [20]) as a *Redheffer Star Product,* [17] and denoted as $\boldsymbol{G^n} * \boldsymbol{G^{n+5}}$. A long stretch of the channel flow is obtained as a chain of star products,

$$\boldsymbol{G^{n-5N_1}}(s) * \cdots * \boldsymbol{G^n}(s) * \boldsymbol{G^{n+5}}(s) * \cdots * \boldsymbol{G^{n+5N_2}}(s). \tag{17}$$

Theoretically, a state-space representation of a channel could now be built up this way, but, essentially, this would require the storage of enormous amount of data which would be of little use afterwards. Instead, we shall store only frequency domain data, so the above cascade of star products is computed pointwise, for a finite set of $\{j\omega_i, i = 1, \ldots K\}$. Note that star-product over complex matrices is a simple operation. Low-order transfer

functions from the boundary input to the shear output will be fitted on this frequency-domain data.

The boundary conditions at the up- and down-stream ends of the channel can be described as transfer function matrices from $\boldsymbol{v}_{\boldsymbol{ob}}^{\boldsymbol{n-5N_1}}$ to $\boldsymbol{v}_{\boldsymbol{ib}}^{\boldsymbol{n-5N_1}}$ and $\boldsymbol{v}_{\boldsymbol{of}}^{\boldsymbol{n+5N_2}}$ to $\boldsymbol{v}_{\boldsymbol{if}}^{\boldsymbol{n+5N_2}}$, respectively. In our case, we leave them zero and consider a channel sufficiently long that the conditions at its ends have an negligible effect on the relevant mid-section. Note also that if we connected $\boldsymbol{v}_{\boldsymbol{ib}}^{\boldsymbol{n-5N_1}}$ with $\boldsymbol{v}_{\boldsymbol{of}}^{\boldsymbol{n+5N_2}}$ and $\boldsymbol{v}_{\boldsymbol{if}}^{\boldsymbol{n+5N_2}}$ with $\boldsymbol{v}_{\boldsymbol{ob}}^{\boldsymbol{n-5N_1}}$ we would obtain the periodic case, studied in [4], [6], [15], [16].

We assume that the dynamics of the actuator is described by a simple model of a pump, given by

$$\dot{\boldsymbol{x}}_{\boldsymbol{p}} = \boldsymbol{A}_{\boldsymbol{p}}\boldsymbol{x}_{\boldsymbol{p}} + \boldsymbol{B}_{\boldsymbol{p}}u, \quad q = \boldsymbol{C}_{\boldsymbol{p}}\boldsymbol{x}_{\boldsymbol{p}} \tag{18}$$

where u is the control input. The derivative of q is then obtained as

$$\dot{q} = \boldsymbol{C}_{\boldsymbol{p}}\boldsymbol{A}_{\boldsymbol{p}}\boldsymbol{x}_{\boldsymbol{p}} + \boldsymbol{C}_{\boldsymbol{p}}\boldsymbol{B}_{\boldsymbol{p}}u \tag{19}$$

In the following, we take as a representative case $\boldsymbol{A_p} = -1$, $\boldsymbol{B_p} = 100$ and $\boldsymbol{C_p} = 1$.

The Reynolds number is taken as $\mathrm{Re} = 10^4$. This is the Reynolds number used in the other studies referenced above. It is chosen as it is greater than the critical Reynolds number for this problem of 5772, where the flow is known to be unstable to small 2-D disturbances with a range of wave numbers and frequencies. Hence it provides a suitable test case.

For the controlled boundary condition, we assume that $dl(x)/dx$ takes the form of a pair of opposed rectangular pulses. Specifically

$$\frac{dl(x)}{dx} = \begin{cases} 1 & x \in \left[x_0 - \frac{\pi}{2}, x_0\right] \\ -1 & x \in \left[x_0 + \frac{\pi}{2}, x_0 + \pi\right] \\ 0 & \text{elsewhere.} \end{cases} \tag{20}$$

The function $l(x)$ is zero at the upstream end. The distance between centers of these pulses equals to π which corresponds to the half wavelength of one of the growing spatial modes. This function is a model of a pair of blowing/suction panels which are under development and considered for use in the aerospace industry. Strictly speaking, this function is not smooth and hence the solution of the PDE (6) has singularities at points where $dl(x)/dx$ is not continuous. Because of the nonzero grid size, the numerical procedure smoothes these singularities, and in practice no special account needs to be taken of them. However, the immediate neighborhood of these points must be avoided when placing shear sensors, as the solution there is likely to have a high relative amount of numerical error.

The use of coupled panels guarantees zero total mass of transpired fluid at each time instant. This zero-mass condition is necessary in the periodic setting, but not here with the finite-difference representation of the spatial dependence of the flow. We shall, however, preserve it here. Note, however, that we have also considered systems with independent panels with nonzero mass flux, and found that n pairs of coupled blowing/suction panels with zero total mass of transpired fluid handles disturbances more effectively than n independent panels while using models and systems of approximately equal complexities.

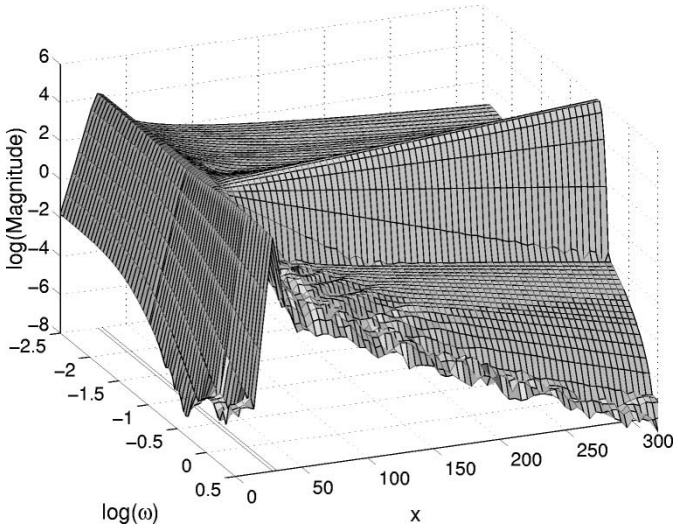

Fig. 3. Magnitude plot for shear along the channel flow. Dashed line shows the positions of the blowing/suction panels.

The grid size was chosen as $\delta = \pi/50$ which produces frequency output data nearly identical to those of $\delta = \pi/100$ and $\pi/200$-naturally, except for the segments containing singularities. The scaling involving the π factor was chosen because of the fact that one of the fundamental wavenumbers has length 2π. The Chebyshev order is taken as $M = 40$ and an analysis in [4] (where the periodic case was treated) shows that this is sufficiently accurate for frequency range of up to one radian. The control design developed below is within this range.

The transfer function matrix from the pump input u to the wall-shear stress is denoted by $G_{uz}(s, x - x_0)$. Its frequency domain representation $G_{uz}(j\omega, x - x_0)$ is obtained by a procedure based on a string of star products discussed above. The data available are for $x \in [0,100\pi]$, sampled at intervals of five-times the grid length. To eliminate the effect of the boundary condition at the upstream and downstream ends of the channel, we added another 100π-long segment of channel to each end. Somewhat arbitrarily the position of the blowing/suction panels was taken as $x_0 = 9\pi$.

A three-dimensional plot of the shear magnitudes $|G_{uz}(j\omega, x - x_0)|$ is shown in Fig. 3. In accordance with intuition, the actuator has very little affect on the upstream flow, but also as expected, it has a significant affect on the flow downstream of the actuation. The control-to-shear gain grows in a band where $\omega \approx [0.17, 0.27]$, with the maximum growth rate at $\omega \approx 0.22$. Elsewhere, the gain is (almost monotonically) decreasing. Fig. 4 shows Bode plots computed at three different locations downstream from the panels. The magnitude-phase plot for fixed $\omega = 0.22$ along the x axis is shown in Fig. 5, from which it can be seen that for large x the amplitude grows exponentially. The growth rate of about 1.08 every 2π is close to the maximum growth with x for individual frequencies. The phase decreases linearly with x. It can be seen from Fig. 4 that the phase decreases by approximately 9000 degrees over a distance of 170, which gives a wavelength somewhat below 2π for this ω. These observations are consistent with the properties of solutions to the *Orr-Sommerfeld equation* (see later) which governs linear normal mode disturbances to 2-D parallel flow.

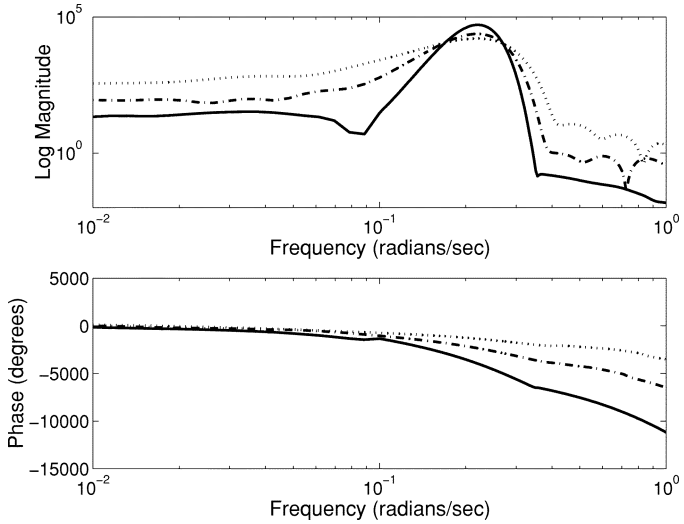

Fig. 4. Bode plot for shear transfer function at $x = x_0 + 10\pi$ (dotted), $x_0 + 20\pi$ (dash-dot) and $x_0 + 40\pi$ (solid).

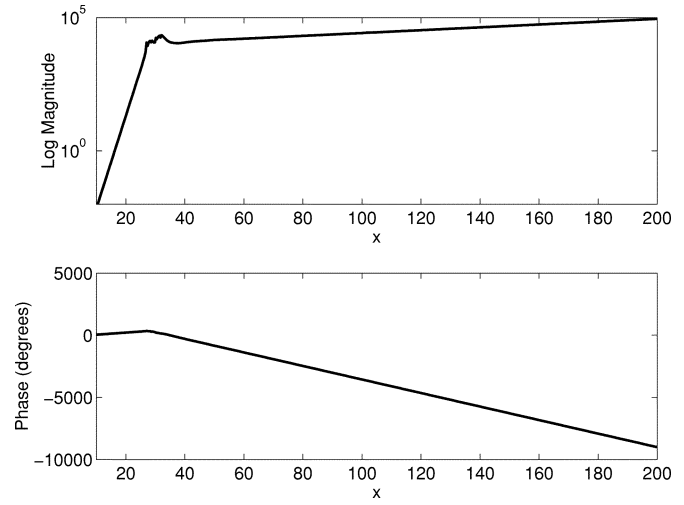

Fig. 5. Magnitude-phase plot along the x-axis for fixed $\omega = 0.22$.

For a frequency of $\omega = 0.22$, the Orr-Sommerfeld solution predicts a growth rate of 1.08 every 2π, and phase change of approximately 9240 degrees over a distance of 170. Both of these are consistent with the results shown in Fig. 5. Further, an Orr-Sommerfeld analysis predicts instability in the range $\omega \approx [0.17, 0.27]$, as found here. Hence, the modeling (and model order reduction procedure) used in this paper produces results consistent with the basic physics of the flow. Note that we do not assume that the disturbance has normal mode form, but allow the perturbation to the mean flow to evolve from upstream excitation in the form of surface transpiration, assuming only that the flow is 2-D and that problem can be linearized.

B. Fitting a Transfer Function Matrix and Uncertainty Bound on Frequency-Domain Data

Consider a set of k sensors regularly spaced at intervals of δ_s and a set of m panel-pairs with a distance δ_p between their centers. The corresponding transfer function matrix can be computed for $i = 1, \ldots, k$; $j = 1, \ldots m$ as

$$\boldsymbol{G_{uz}}(s) = [G_{uz}(s, x + (i-1)\delta_s + (1-j)\delta_p - x_0)] \quad (21)$$

where the scalar transfer function $G_{uz}(s, \cdot)$ is as in Section II-A; x is now fixed and describes the position of the most upstream sensor relative to x_0 in (20) for the most upstream panel pair. In what follows we shall consider $\delta_s = \delta_p = 2\pi$. This separation between panel pairs/sensors is chosen so that the controller can most efficiently attack disturbances of wavelengths around 2π. The distance x was chosen as $x = 2.3\pi$.

Each of the above transfer functions is chosen as an N_{ij}-order proper rational function. To obtain an approximation of the i-th row in $G_{uz}(s)$ we can use the function `fitsys` of the μ-toolbox for MATLAB, see [1]. This function performs *weighted least square fitting*. As we deal with computational and not experimental data, we can assume arbitrarily many data points. Also, we assume that these data are not corrupted by noise, which greatly simplifies the modeling. In this case, noise would be just computational round-off errors which are deemed to be small compared to the modeling error arising from approximation of an infinite-dimensional system (or its high-dimensional approximation) by a low-order transfer function. The frequency-dependent weight was chosen as $|(30j\omega + 1)/(2.5j\omega + 1)^2|$ which emphasizes the frequency range of $[0.03, 0.4]$ which contains the range of spatial growth. The orders were chosen as 8, 10, 12, 16 for the respective rows of $\boldsymbol{G_{uz}(s)}$ which fits the data fairly accurately. The transfer functions were converted to state-space representations which were used later in the control design. During this procedure we have to ensure that the resulting models are stable, in accordance with the behavior of the real system (in this setting the flow trajectories grow spatially but not temporally for fixed x). If the approximation order is too high, the procedure may result in models with almost cancelled unstable zero-pole pairs.

The basic premise on which the controllers used in this work are designed is that the underlying dynamics can be approximated by a relatively low-order transfer function coupled with an uncertainty description which, in essence, is a parameterization of the unmodeled dynamics. This problem is at the heart of robust control and a rich theory exists based on different models for describing the uncertainty and is extensively covered in the relevant technical literature which includes texts such as [20]. The basic point now is to obtain the components of this overall description, i.e., the nominal model and the uncertainty description, and then to proceed to controller design. Here we use the left-coprime factor uncertainty description (but others could also be considered).

Let the low-order representation of the flow, obtained from the fitting procedure be $\hat{\boldsymbol{G}}_{\boldsymbol{uz}}(s)$ and write its left-coprime factorization as $\hat{\boldsymbol{G}}_{\boldsymbol{uz}}(s) = \boldsymbol{M}(s)^{-1}\boldsymbol{N}(s)$. One possible choice here is the *normalized left-coprime factorization*. We then consider the model set

$$\Big\{(M + W_1\Delta_1 W_2)^{-1}(N + W_1\Delta_2 W_3) : \Delta_1, \Delta_2 \text{ stable}, \|[\Delta_1, \Delta_2]\|_\infty < 1\Big\} \quad (22)$$

where $\boldsymbol{W_1}, \boldsymbol{W_2}, \boldsymbol{W_3}$ are stable and minimum phase weighting matrices. First, we shall consider the following problem: given fixed weights and set of frequency points $\{\omega_i\}_{i=1}^k$, are the data $\boldsymbol{G_{uz}}(j\omega_i)$, $i = 1, \ldots K$ consistent with the model (22). As is well known, even if the model is consistent, i.e., there is a feasible uncertainty such that

$$\begin{aligned}\boldsymbol{G_{uz}}(j\omega_i) = &\left(\boldsymbol{M}(j\omega_i) + \boldsymbol{W_1\Delta_1 W_2}(j\omega_i)\right)^{-1} \\ &\times \left(\boldsymbol{N}(j\omega_i) + \boldsymbol{W_1\Delta_2 W_3}(j\omega_i)\right), \\ &i = 1, \ldots K \end{aligned} \tag{23}$$

it does not imply that the model (22) is valid—no finite set of data can validate a model. We can only suppose that if the model is not invalidated for a sufficiently large and carefully chosen data set, it is very likely valid. This problem is, in a more general setting, and under the presence of measurement noise, solved in [8]. The main result of the work in [8]is, that checking the consistency of a frequency-domain, noise corrupted data set with a general class of uncertain models, requires the solution of a set of K independent linear matrix inequalities (LMIs). As we consider only a noise-free case, this result would reduce to K positive-semidefiniteness tests. The result for the coprime-factor uncertainty case considered in the current work can be formulated in an even simpler manner than in [8]as follows:

Theorem 1: Assume that $\boldsymbol{M}(s)^{-1}$ is stable and $\|\boldsymbol{W_1\Delta_1 W_2}\|_\infty < 1$. The data $\boldsymbol{G_{uz}}(j\omega_i)$, $i = 1, \ldots K$ are consistent with the model (22) iff

$$\begin{bmatrix} \boldsymbol{W_{3i}^* W_{3i}} + \boldsymbol{G_{uzi}^* W_{2i}^* W_{2i} G_{uzi}} & \boldsymbol{M_i^* G_{uzi}^* - N_i^*} \\ \boldsymbol{G_{uzi} M_i - N_i} & \boldsymbol{W_{1i} W_{1i}^*} \end{bmatrix} \geq \boldsymbol{0}, \quad i = 1, \ldots K \tag{24}$$

where the subscript i stands for the argument $j\omega_i$ and the symbol $*$ denotes conjugate transpose.

The proof is based on Lemma 4.3 and the arguments of Theorem 4.1 in [8]. This result is critically important as it provides the essential theoretical basis which guarantees that a model structure of the form used here actually exists.

In the following, for simplicity, we shall restrict ourselves to diagonal weights; moreover, $\boldsymbol{W_1}$ will be constant. For our specific problem we shall consider $\boldsymbol{W_2}$ to be a band-pass; its frequency range will contain the interval of spatial growth, approx 0.17–0.27 radians. Conversely, $\boldsymbol{W_3}$ is a band-stop, stopping these frequencies. The order of the latter filter as well as its maximum gain/minimum gain ratio is higher than in the case of $\boldsymbol{W_2}$. This is because we *a priori* assume that the low-order model is more accurate in the growth interval than elsewhere (which was enforced by the weighting in the least-square fitting). In this setting, H_∞ control syntheses will yield control restricted to this narrow frequency range. This is not a serious restriction for the 2-D disturbances considered here—for other frequencies the disturbances are not spatially growing and hence relatively harmless. The frequency set consists of 320 unevenly distributed points, with 240 of them concentrated between 0.1 and 1.

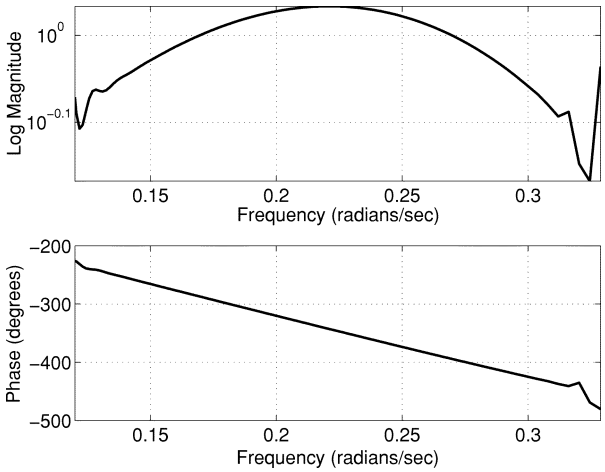

Fig. 6. Bode plot of $F_{2\pi}(j\omega, 100\pi)$.

To obtain tighter bounds, we can apply a minimization procedure: We set $\boldsymbol{W_1}(s) = \boldsymbol{W_1'}(s)\boldsymbol{Q_1}$, $\boldsymbol{W_2}(s) = \boldsymbol{Q_2 W_2'}(s)$, and $\boldsymbol{W_3}(s) = \boldsymbol{Q_3 W_3'}(s)$. Here, $\boldsymbol{W_1'}, \boldsymbol{W_2'}, \boldsymbol{W_3'}$ are weights for which the model (22) is not invalidated and $\boldsymbol{Q_1}$, $\boldsymbol{Q_2}$, and $\boldsymbol{Q_3}$ are constant diagonal matrices. On substitution into (24), we obtain an LMI constraint for variables $\boldsymbol{S_1} = \boldsymbol{Q_1 Q_1^T}$, $\boldsymbol{S_2} = \boldsymbol{Q_2^T Q_2}$ and $\boldsymbol{S_3} = \boldsymbol{Q_3^T Q_3}$. Further constraints are $\boldsymbol{0} < \boldsymbol{S_k} \leq \boldsymbol{I}$, $k = 1, 2, 3$. The cost function to be minimized is $\sum_{i=1}^3 \alpha_i \mathrm{trace}(\boldsymbol{S_i})$ where α_i, $i = 1, 2, 3$ are weights. This optimization is done using the mincx function of the LMI Control Toolbox, see [11].

C. Disturbance Model

For control system design we need a disturbance model. Although its accuracy does not affect the closed-loop stability (and hence its error is not included to the overall modeling uncertainty) it is important for performance. First we consider this problem: If we measure the shear disturbance at a point x, can we estimate the value of shear at $x + \Delta_x$ at the same time? The answer is yes, provided it is sufficiently far downstream from its source. Let

$$F_{\Delta_x}(s, x) = \frac{G_{uz}(s, x + \Delta_x)}{G_{uz}(s, x)}. \tag{25}$$

A Bode plot of this transfer function (for $x \approx 100\pi$) and $\Delta_x = 2\pi$ is shown in Fig. 6. First, in the ω-interval approx. $[0.15, 0.3]$ the phase is a linear function of ω, and the magnitude is a concave function of ω with a maximum of approximately 1.08 for $\omega \approx 0.22$. This corresponds to the growth rate $\exp(0.012x)$. The interval where the magnitude is greater than 0dB is the interval of spatial growth. These frequency responses are, for $\omega \in [0.15, 0.3]$, invariant of the base value of x, provided it is sufficiently far downstream from the panels. For ω outside this region the disturbance behavior is complex, highly x-dependent and hence hard to predict. Note, however, that for control design purposes we do not need to deal with disturbances which are spatially decreasing. Therefore, we fit a stable 4th-order transfer function $\hat{F}_{2\pi}(s)$ to the frequency-domain data in the interval between 0.15 and 0.3. Assuming that z_i is shear disturbance measured at $x = x_i$, $\hat{F}_{2\pi}(s)z_i$ is our estimate for shear at $x_i + 2\pi$.

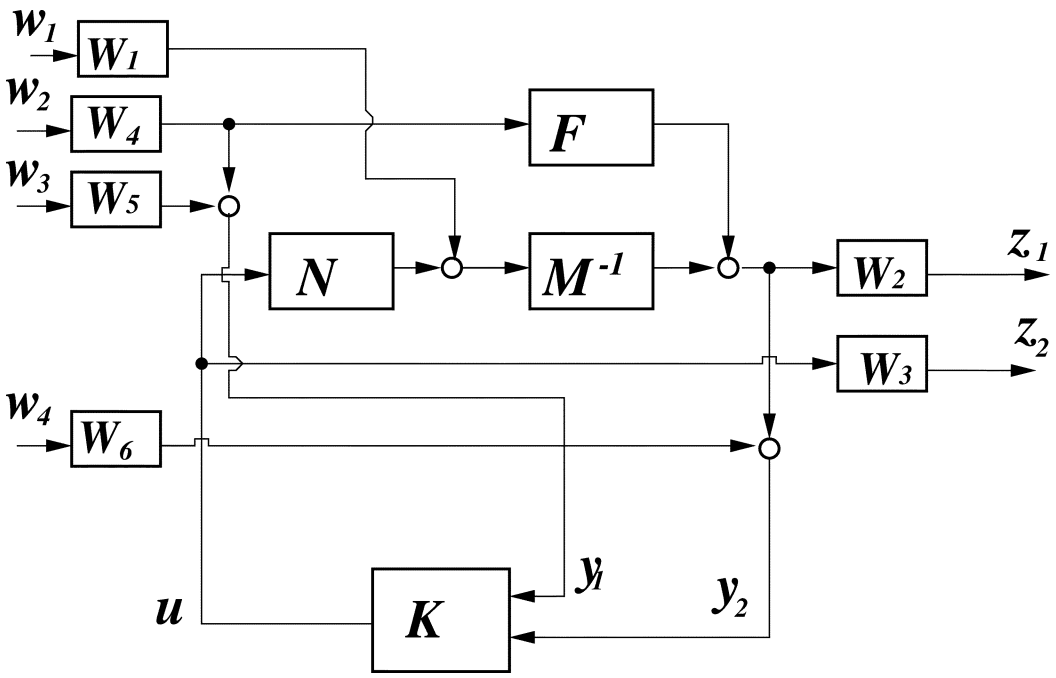

Fig. 7. Control configuration.

Time-domain simulations showed that this simple model estimates the advance of the waves remarkably well, regardless of the value of x_i.

For a more efficient disturbance attenuation we shall add an additional sensor 4π upstream from the first sensor considered in Section II-B. This is far enough upstream from all panels so that the effect of wall transpiration on this sensor's measurements is negligible. It measures directly the oncoming disturbance (assuming the measurement noise is also negligible in the relevant frequency range). The overall disturbance transfer function matrix from the shear measured far upstream to disturbances at the other sensors is then given by

$$\boldsymbol{F}(s) = \left(\hat{F}_{2\pi}(s)^2 \begin{bmatrix} 1 & \hat{F}_2\pi(s) & \hat{F}_{2\pi}(s)^2 & \hat{F}_{2\pi}(s)^3 \end{bmatrix}\right)^T. \tag{26}$$

The state-space realization of this disturbance model has dimension 20.

III. Control Design and Simulations

A. Control Problem Formulation

The control configuration in the H_∞ control setting is shown in Fig. 7. There are four external inputs—$\boldsymbol{w_1}$ disturbs the coprime-factor model, w_2 generates the flow disturbance measured at the far upstream sensor; w_3 and $\boldsymbol{w_4}$ are measurement noises. Disturbance w_2 is filtered through $W_4(s)$ which passes only the frequencies around the growth region and enters the disturbance model $\boldsymbol{F}(s)$, as discussed in Section II. This filtered disturbance is also mixed with scaled noise $W_5 w_3$ and fed to the controller as measurement y_1. The measurements from the other sensors are corrupted by the noise $\boldsymbol{W_6 w_4}$ and fed to the controller as $\boldsymbol{y_2}$. The penalized outputs $\boldsymbol{z_1}$, $\boldsymbol{z_2}$ are filtered shear measurements and controls, respectively. The weights $\boldsymbol{W_1}, \boldsymbol{W_2}$, $\boldsymbol{W_3}$ were discussed in Section II. We chose $\boldsymbol{W_1}(s) = \boldsymbol{Q_1}$, $\boldsymbol{W_2}(s) = \boldsymbol{Q_2} w_2(s)$, $\boldsymbol{W_3}(s) = \boldsymbol{Q_3} w_3(s)$, where $\boldsymbol{Q_1}, \boldsymbol{Q_2}, \boldsymbol{Q_3}$ are constant diagonal scaling matrices. Specifically

$$\begin{aligned} w_2(s) &= \frac{2.8 \cdot 10^4 (s + 2.135)(s + 0.0248)}{(s^2 + 0.2847s + 0.2)} \\ &\quad \times \frac{(s^2 + 2.136s + 4.7197)}{(s^2 + 0.36s + 0.0529)} \\ &\quad \times \frac{(s^2 + 0.0239s + 6 \cdot 10^{-4})}{(s^2 + 0.0753s + 0.014)} \\ w_3(s) &= 5.12 \cdot 10^5 W_4(s)^{-3} \\ Q_1 &= 10^{-3} \mathrm{diag}([2.2, 3.1, 3.2, 2.4]) \\ Q_2 &= \mathrm{diag}([2.4, 2, .4, 2, 3.27]) \\ Q_3 &= \mathrm{diag}([1.95, 2.5, 1.72, 1.44]). \end{aligned}$$

Finally

$$W_4(s) = \frac{2(s^2 + 1.349s + 1.007)(s^2 + 0.0649s + 0.0023)}{(s^2 + 0.0382s + .0569)(s^2 + 0.0325s + 0.0412)}$$

$W_5 = 20\sqrt{2}$ and $\boldsymbol{W_6} = 20\boldsymbol{I_4}$. Magnitude plots of the frequency-dependent weights are shown in Fig. 8. For this weight combination, the model set (22) is consistent with our extensive data set. To guarantee robust stability for this set of plants it is sufficient that the H_∞ performance index is less than 1. For the above problem formulation we found a controller which guarantees the H_∞ performance index $\gamma = 0.945$. It was computed by the `hinfsyn` routine of the μ-analysis/synthesis toolbox, [1].

The plant order is 142, where the order of the model describing the relation between control and measured shear is 46, the order of the disturbance model is 20, and the rest account for the weights. This will result in a controller of the same order, which is very high for implementation in practice. However, it

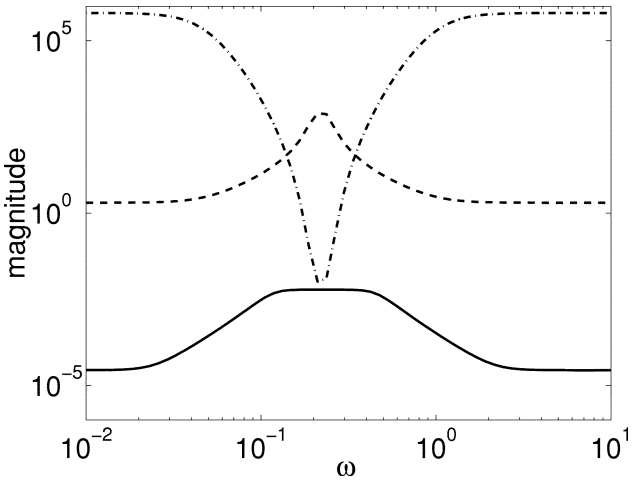

Fig. 8. Magnitudes of weights $w_2(s)$ (solid), $w_3(s)$ (dashed), $W_4(s)$ (dash-dotted).

can be readily reduced by the Hankel-optimal reduction procedure [12] to 32, which is practically feasible, with no performance degradation. Further reduction to 24 results in a slight but acceptable performance degradation.

B. Closed-Loop Frequency-Domain Analysis

In this section we shall consider the full-order controller. For the frequency-domain analysis, the disturbance has been simulated as an action of a pair of blowing-suction panels (the same as those used for control) placed about 80π upstream from the panels. Fig. 9 shows the magnitude of this shear disturbance around the uncontrolled section (top) and the shear at the same channel section when the control actuation is applied (bottom). Only the frequencies around the growth interval are shown—elsewhere there is no significant difference between these two cases. Note that the controller reduces shear significantly at the sensor locations and further downstream. Note also that the design directly penalizes shear only at the four points where the sensors are placed.

We can observe slight disturbance amplifications at the locations of the panels. However, this is compensated by significant shear reductions downstream which occurs at all frequencies of the growth region. The magnitude versus distance plot for fixed frequency ω is given in Fig. 10, with the magnitude in this plot scaled linearly. The positions of panels and sensors are also shown in this figure.

As expected, at the sensor locations the shear is reduced much more than elsewhere. Nevertheless we can see that, as desired, the controller also reduces shear significantly far downstream from the sensor position. As expected, downstream of the actuation the shear disturbance resumes its original growth rate, but it would take a very long stretch of the channel to restore it to the size it had before entering the controlled area. Finally, a comparison of magnitude plots for uncontrolled/controlled shear downstream from the controlled area is given in Fig. 11. The uncontrolled-to-controlled shear ratio is nearly constant for all locations at least 10π downstream from the panels, further demonstrating that the disturbance has in fact resumed its original growth rate, albeit at a lower magnitude.

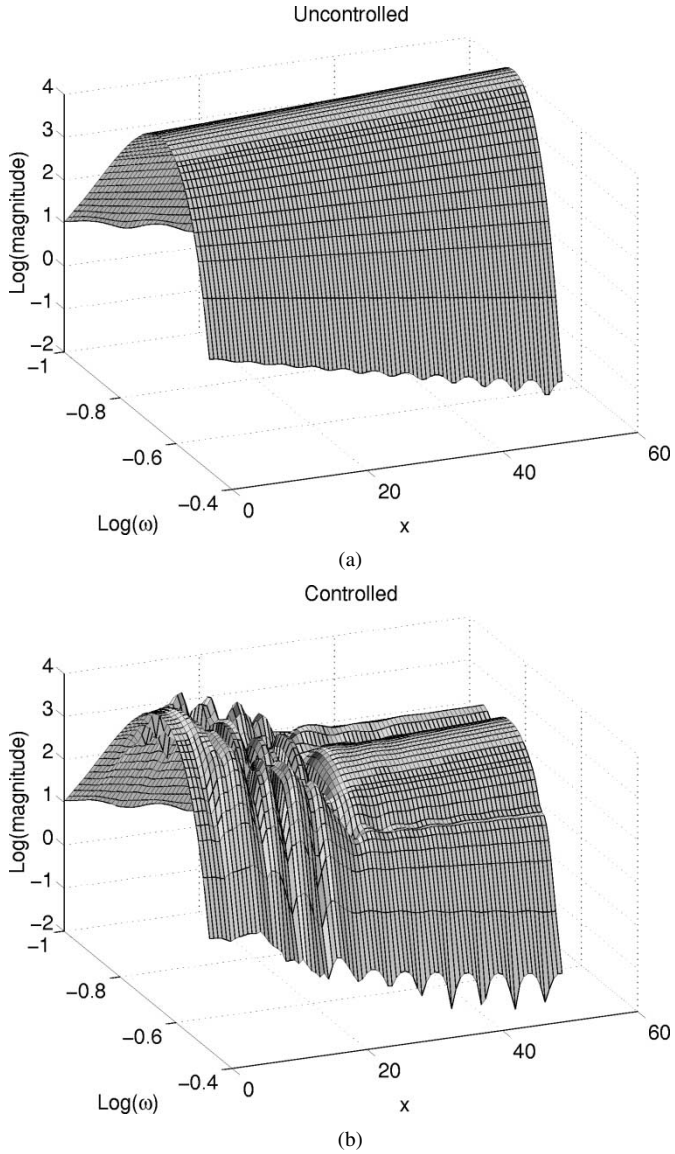

Fig. 9. Uncontrolled (top) and controlled (bottom) shear response.

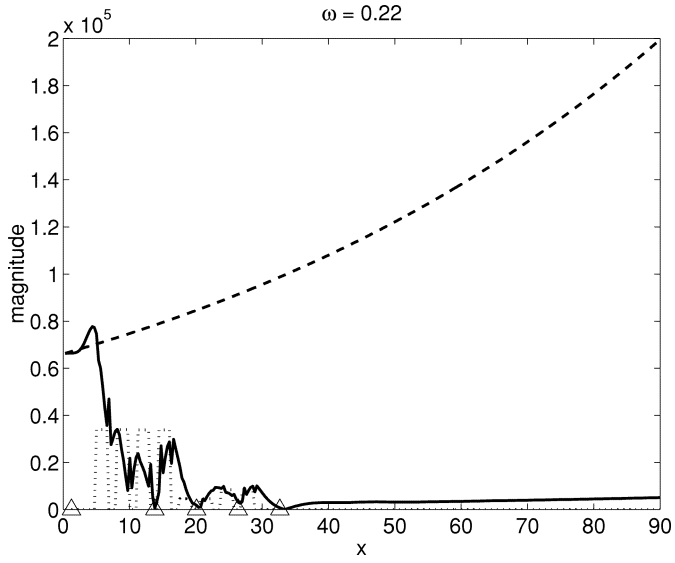

Fig. 10. Magnitude versus distance: controlled shear (solid), uncontrolled shear disturbance (dashed), control multiplied by 10^4 (dotted); triangles: positions of the sensors.

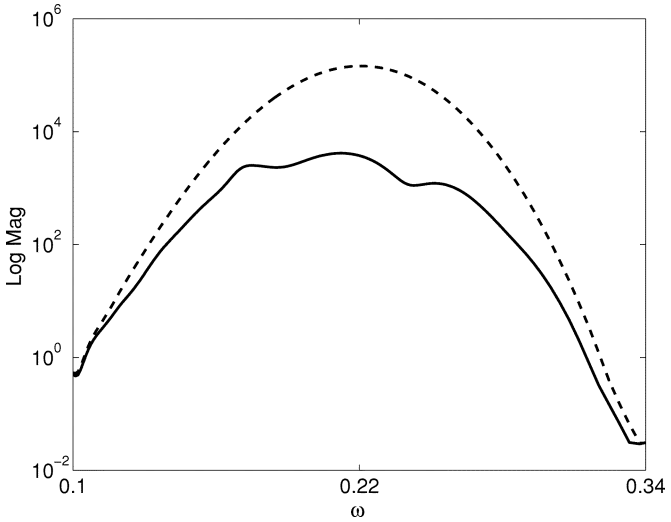

Fig. 11. Magnitude plots of uncontrolled (dashed) and controlled shear disturbance in the distance of about 20π downstream from the sensors and actuators.

C. CFD Evaluations

The controller was tested by incorporating it in a closed-loop simulation with a 2-D nonlinear Navier–Stokes solver. This CFD (*Computational Fluid Dynamics*) code solves the nonlinear Navier–Stokes equations, given for 2-D flow in streamfunction form as

$$\frac{\partial}{\partial t}\nabla^2\psi + u\frac{\partial}{\partial x}\nabla^2\psi + v\frac{\partial}{\partial y}\nabla^2\psi = \frac{1}{Re}\nabla^4\psi \tag{27}$$

where ψ is the streamfunction and

$$(u, v) = \left(\frac{\partial\psi}{\partial y}, -\frac{\partial\psi}{\partial x}\right). \tag{28}$$

Equation (27) is the nonlinear version of (6) minus the forcing terms, which arise from the use of the modified streamfunction Φ as defined in (4) and (5) rather than the usual form of the streamfunction as given in (28). The modified streamfunction is used above for numerical convenience as it gives homogeneous boundary conditions. With ψ the boundary conditions are inhomogeneous, given by

$$\psi = q(t)l(x) \text{ and } \frac{\partial\psi}{\partial y} = 0 \text{ at } y = -1 \tag{29}$$

$$\psi = \frac{\partial\psi}{\partial y} = 0 \text{ at } y = 1. \tag{30}$$

Note that with this formulation the only assumption made is that the flow is 2-D, and that interactions between the various possible modes in the flow are allowed, including generation of an infinite sequence of modes of different wavelengths due to the nonlinear terms. Also, there is no inherent restriction to small disturbances, although it is our aim to prevent the growth of both disturbances which are introduced deliberately, as in the frequency domain analysis above and at the upstream end of the channel as below, and those generated through interactions in the flow.

The code used to solve the system of (27)–(30) is an implicit finite difference code which is fourth order in space and second order in time. It was developed specifically for channel flow problems of this kind. Full details of the code can be found in [19].

A number of different disturbances were considered, including those generated by a pair of suction/blowing panels, similar to the procedure used in the frequency domain analysis described above. Also, disturbances were generated at the inlet (the upstream end of the channel) using a combination of Orr-Sommerfeld modes, a procedure that will now be described. A disturbance to the flow for a single wavenumber takes the form

$$\psi_1 = \mathcal{R}e\left[\phi(y)\exp(j(\alpha x - \omega t))\right] \tag{31}$$

where ψ_1 is the perturbation streamfunction, ϕ is its complex amplitude, and α and ω are the wave number and frequency of the disturbance. In generating the Orr-Sommerfeld notes, ϕ is assumed to be sufficiently small that the governing Navier-Stokes (27) can be linearized. Hence ϕ satisfies a fourth-order ODE (the Orr-Sommerfeld equation)

$$\left(U - \frac{\omega}{\alpha}\right)(\phi'' - \alpha^2\phi) - U''\phi + \frac{j}{\alpha\mathrm{Re}} \times(\phi'''' - 2\alpha^2\phi'' + \alpha^4\phi) = 0 \tag{32}$$

where the prime denote differentiation with respect to y. ϕ satisfies homogeneous boundary conditions: $\phi = \phi' = 0$ at $y = \pm 1$. This problem is a eigenvalue problem, where for our application the Reynolds number of the flow and the frequency of the disturbance ω are chosen, and the complex wavenumber $\alpha = \alpha_r + j\alpha_j$ is the eigenvalue which is calculated as part of the solution. Further information of the Orr-Sommerfeld equation and its applications can be found in [10] or [18].

Here the value of ω is adjusted to give the desired real part of the wave number α_r, which determines the wavelength of the disturbance. The complex part of α, α_j, gives the growth rate of the disturbance. The disturbance was then generated at the inlet from (31) by setting $x = 0$ and adding the time varying perturbation to Poiseuille flow.

Two different disturbances of this type where considered. The first has a single Orr–Sommerfeld mode with $\alpha_r = 1$, giving a disturbance which grows slowly in x. The spatial distribution of the wall shear stress for this disturbance once the control system has had time to come fully into play is shown in Fig. 12. Note here that the actuation is extremely small. The disturbance shown in Fig. 12 is $O(2.5 \times 10^{-3})$ relative to the shear of the base Poiseuille flow ($\partial U/\partial y = 2$ at $y = -1$), while the actuation is two orders of magnitude less, i.e., $v_w = O(5 \times 10^{-5})$ against $U(0) = 1$. It is clear that, even under these condition, which are stricter and more realistic than those used in the controller design phase, the controller produces a drastic reduction in the shear. In Fig. 12 the disturbance downstream of the actuators appears to be growing again. This is as expected as there is no way in practice of completely eliminating the unstable mode from the problem. However, the disturbance could be kept at a low level by cascading controllers, i.e., by introducing independent blocks of the control system at widely spaced intervals along the channel.

Fig. 13 shows shear measurements against time at sensor 5 (placed upstream of the actuation so that it measures the

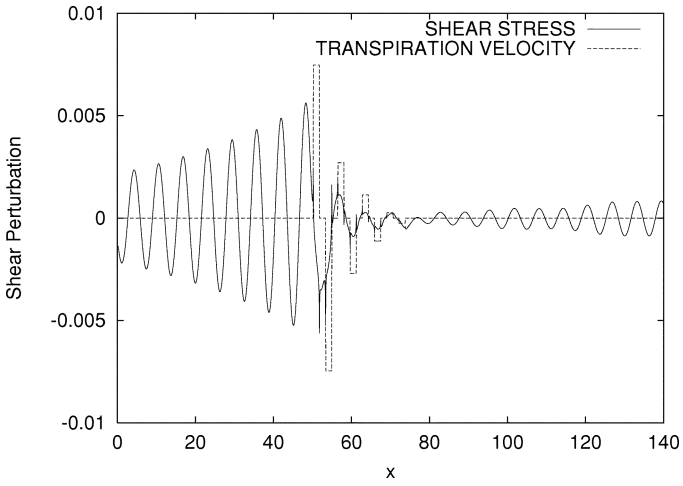

Fig. 12. Shear stress perturbation and transpiration velocity (scaled by $\mathrm{Re}/48$) along the lower wall and at single instant in time. The disturbance is a single mode with wavenumber α_r.

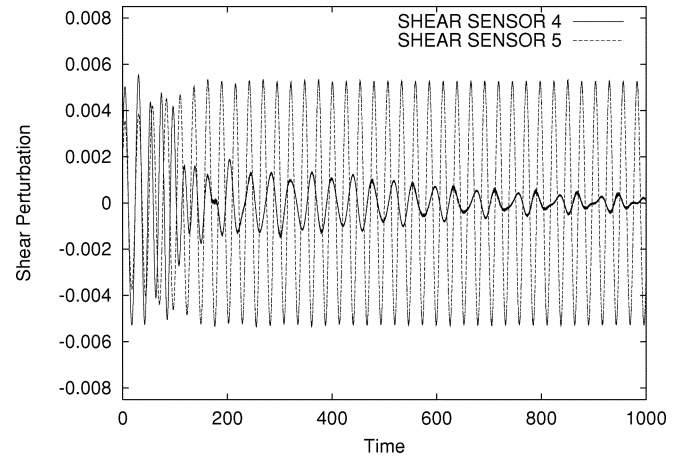

Fig. 13. Shear stress perturbation against time for the single wavenumber disturbance, measured at further upstream (ahead of the actuation) and downstream (behind the actuation) sensors.

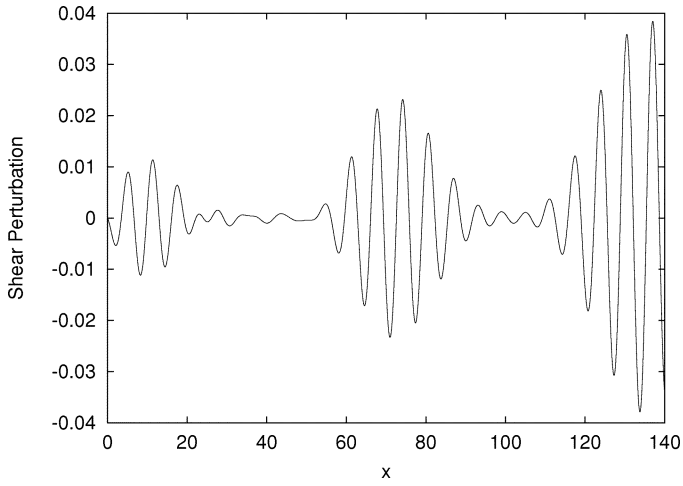

Fig. 14. Shear stress perturbation on the lower wall for an uncontrolled disturbance at one instant in time. The disturbance is multiple mode with wavenumbers $\alpha_r = 0.8$, 0.9, 1.0, 1.1, and 1.2.

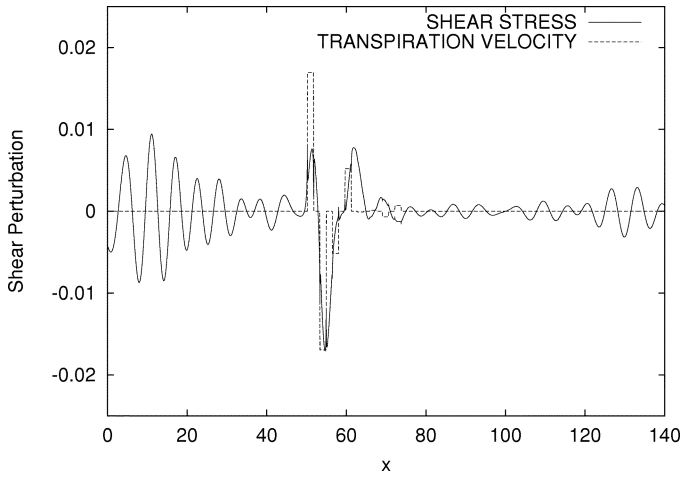

Fig. 15. Shear stress perturbation and transpiration velocity (scaled by $\mathrm{Re}/24$) on the lower wall at one instant in time. The disturbance is multiple mode with wavenumbers $\alpha_r = 0.8$, 0.9, 1.0, 1.1, and 1.2.

oncoming disturbance) and sensor 4 (the furthest downstream, after the actuation). As in Fig. 12, this shows a large reduction in the disturbance across the region containing the actuation. In fact, this figure understates the amount of shear reduction as the uncontrolled disturbance arriving at sensor 4 would be approximately 40% larger than that measured at sensor 5 due to its exponential growth. Also, from Fig. 13 we can see that although the incoming disturbance settles on a constant amplitude reasonably early in the run, the amplitude is still decaying at sensor 4, even at $t = 1000$. This decay continues until $t \approx 1500$, after which the signal from sensor 4 settles.

The calculations performed to generate Figs. 12 and 13 involved determining iteratively approximately 350 000 unknown variables each time step, where the time step was 0.025. In contrast,the full order controller has 142 states. Hence, the computational effort in calculating the new suction/blowing velocities at each time step is insignificant, and generating a low-order controller is not strictly necessary in order to perform simulations such as those presented here. Note, i.e., however that this does not imply a lower order controller would not be required if the controllers were to be implemented experimentally.

The second disturbance of this type used a combination of five Orr-Sommerfeld modes with $\alpha_r = 0.8$, 0.9, 1.0, 1.1, and 1.2., which has two modes which grow spatially, two which are decaying and one with close to zero growth rate. Further, each of the modes was given the same magnitude at the inlet so that the total disturbance had the form of a wave packet which is modulated as it propagates downstream, as shown in Fig. 14. This disturbance gives not only a combination of wavelengths, which should provide a sterner test of the controller, but a simple model of an intermittent disturbance. Intermittent disturbances are of considerable practical significance as they are commonly seen in transitional flows (see, e.g., [18]). Figs. 15 and 16 show the results for this multiple-wavenumber disturbance. Again, the controller is performing satisfactorily, with a large reduction in the shear perturbation.

In the addition to the disturbances based on solutions to the Orr-Sommerfeld equation, disturbances were provoked using a zero mass flux panel pair starting at $x = 20$ where the inlet is at $x = 0$. The first of the panels in the actuation was placed at distance 16π further downstream. The wavelength of the dis-

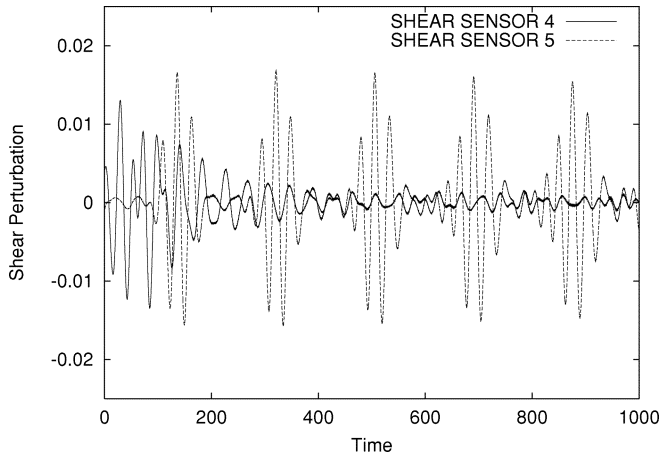

Fig. 16. Shear stress perturbation against time at the furthest upstream and downstream sensors for the disturbance as in Fig. 15.

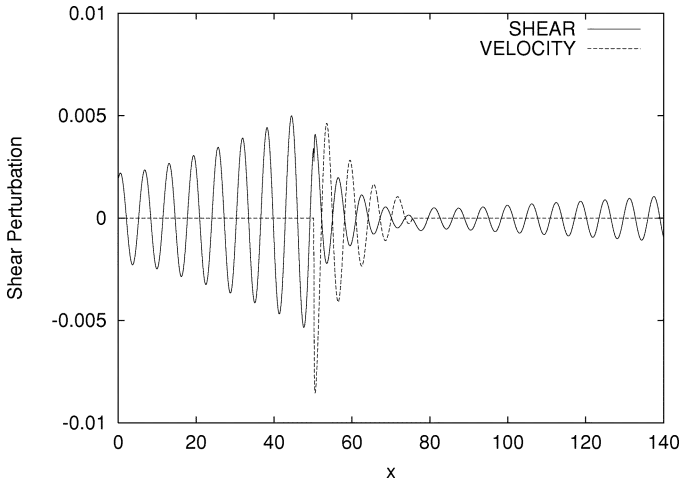

Fig. 17. Shear stress perturbation and transpiration velocity (scaled by $\mathrm{Re}/24$) on the lower wall at one instant in time for a proportional controller with gain -0.005. The disturbance is single mode with wavenumber $\alpha_r = 1$.

turbance generated in this manner was varied by changing the length and distance between the upstream panel pair (the configuration of the actuation sensor system was fixed as given above). Different frequencies of excitation were also used. Further the magnitude of the transpiration on the panels generating the disturbance was varied, from an amplitude which produced a disturbance similar in size to those shown in Figs. 12–16 above, to one several orders of magnitude larger which generated a disturbance with a shear stress perturbation greater than 25% of the mean value. In all these cases, the control system worked in a similar manner to that shown in Figs. 12–16 above, with a significant reduction of the shear downstream to the actuation.

The control system used above was not simple to produce. However, as shown in [15], a simple proportional controller can be used for a model problem with a single unstable mode with $\alpha = 1$. Although the particular control configuration used in [15](sinusoidal transpiration with $\alpha = 1$ and a single sensor based at a point of maximum transpiration) failed in a test when confronted with the multiwavenumber Orr-Sommerfeld type disturbance presented above, there would clearly be advantages in practice if a simple proportional could be used. Hence a number of different configurations with proportional control were investigated. These included zero mass flux discrete panel pairs, in a configuration the same as used above, but with a sensor at the centre of the first panel, and a nonzero mass flux system with independent panels with a sensor at the center of each panel. In the latter case, the panels were either contiguous, or had gaps between them. Different lengths and number of panels were investigated. In addition, a simple point wise proportional controller with

$$v_w(x,t) = -0.005\frac{\partial \hat{u}}{\partial y}(x,-1,t) \tag{33}$$

operating over a distance of 8π, similar to that for the discrete panel control system described earlier. This proportional controller does not guarantee zero mass flux. The gain (-0.005) was chosen through trial and error. Increasing its magnitude significantly (to -0.0075 say) destabilises the entire system and the numerical procedure failed rapidly, while decreasing it produces worse results. The shear on the lower wall obtained when applying this system to the single mode Orr-Sommerfeld type disturbance is shown in Fig. 17. As can be seen by comparing Fig. 12 with Fig. 17, although the proportional controller does significantly reduce the shear stress perturbation it does not perform as well as the discrete panel system used for Fig. 12.

Of all the configurations tested with proportional controllers, the one used for Fig. 17, with continuous sensing and transpiration, produced the best results. In particular, ones with a moderate number of discrete panels, which are the most realistic physically, produced a much lower level of reduction in the wall shear perturbation.

IV. Conclusion

The main contribution of this paper is to (finite-dimensional) modeling and control of spatially growing channel flows. Modeling takes place in the frequency domain using an efficient method of generating spatial frequency responses based on the star product. From the spatial distribution of the magnitude and phase we can obtain important information about the flow's properties. In this paper we considered actuation and sensing based mainly on practical considerations, in the form of discrete suction/blowing panels rather than continuous transpiration as in previous work by other authors. This employed four suitably placed pairs of blowing and suction panels and five shear sensors. Frequency-domain data for fixed sensor locations were used for low-order approximation of the flow model as well as estimating the modeling uncertainty. A standard H_∞ controller was designed for this uncertain system. This design was evaluated by simulations with a CFD code in the loop. These simulations showed that the shear reduction downstream from the panels was significant. Further, in practice the disturbance could be maintained at a low level indefinitely far downstream by repeated implementation of the basic sensor/actuator configuration, with each block acting independently.

We note the frequency domain analysis used here based on the Redheffer Star Product produced a very efficient method of analysing the response of the system. The computational effort is $O(N)$ for the number of streamwise grid points that have actuation and $O(\log N)$ in those that do not (most of them).

Hence it is much less computationally intensive than an equivalent time domain simulation. Finally, we note that the analysis of the system was conducted entirely in terms of its inputs (transpiration velocities) and outputs (shear stress measurements), and could therefore, in principle, be applied to situations where detailed knowledge of the flow is not available, e.g., when using experimental measurements.

REFERENCES

[1] G. A. Balas, J. C. Doyle, K. Glover, A. Packard, and R. Smith, *μ-Analysis and Synthesis Toolbox for Use With MATLAB*: Mathworks Inc., 1998.

[2] A. Balogh, W-J. Liu, and M. Krstic, "Stability enhancement by boundary control in 2D channel flow–Part I: Regularity of solutions," in *Proc. 39th IEEE Conf. Decision Control*, 1999, pp. 2869–2874.

[3] B. Bamieh, F. Paganini, and M. A. Dahleh, "Distributed control of spatially invariant systems," *IEEE Trans. Automat. Contr.*, vol. 47, pp. 1091–1107, 2002.

[4] L. Baramov, O. R. Tutty, and E. Rogers, "Robust control of linearized Poiseuille flow," *AIAA J. Guid. Dyn. Contr.*, vol. 25, pp. 145–151, 2002.

[5] T. R. Bewley, "Flow control: New challenges for a new renaissance," *Prog. Aerosp. Sci.*, vol. 54, pp. 21–58, 2001.

[6] T. R. Bewley and S. liu, "Optimal and robust control and estimation of linear paths to transition," *J. Fluid Mech.*, vol. 365, pp. 305–349, 1998.

[7] C. Canuto, M. Y. Hussaini, A. Quarteroni, and T. A. Zang, *Spectral Methods in Fluid Dynamics*. New-York: Springer-Verlag, 1988.

[8] J. Chen, "Frequency-domain tests for validation of linear fractional uncertain models," *IEEE Trans. Automat. Contr.*, vol. 42, pp. 748–760, 1997.

[9] L. Cortelezzi, J. L. Speyer, K. H., and J. Kim, "Robust reduced-order control of turbulent channel flows via distributed sensors and actuators," in *Proc. 38th IEEE Conf. Decision Control*, 1998, pp. 1906–1911.

[10] P. G. Drazin and W. H. Reid, *Hydrodynamic Stability*. Cambridge, U.K.: Cambridge Univ. Press, 1981.

[11] P. Gahinet, A. Nemirovski, A. J. Laub, and M. Chilai, *LMI Control Toolbox for Use With MATLAB*: Mathworks Inc., 1995.

[12] K. Glover, "All optimal Hankel-norm approximations of linear multivariable systems and their L_∞-error bounds," *Int. J. Contr.*, vol. 39, pp. 1115–1193, 1984.

[13] P. Hackenberg, O. R. Tutty, J.-L. Rioual, and P. A. Nelson, "The automatic control of boundary layer transition—Experiments and computation," *Appl. Sci. Res.*, vol. 54, pp. 293–311, 1995.

[14] H. H. Hu and H. H. Bau, "Feedback control to delay or advance linear loss of stability in planar Poiseuille flow," *Proc. R. Soc. Lond. A*, vol. 447, pp. 299–312, 1994.

[15] S. S. Joshi, J. L. Speyer, and J. Kim, "A system theory approach to the feedback stabilization of infinitesimal and finite-amplitude disturbances in plane Poiseuille flow," *J. Fluid Mech.*, vol. 332, pp. 157–184, 1997.

[16] ——, "Finite dimensional optimal control of Poiseuille flow," *AIAA J. Guid. Control Dyn.*, vol. 22, pp. 340–348, 1999.

[17] R. M. Redheffer, "On a certain linear fractional transformation," *J. Math Phys.*, vol. 39, pp. 269–286, 1960.

[18] P. J. Schmid and D. S. Henningson, *Stability and Transition in Shear Flows*. New York: Springer-Verlag, 2001.

[19] O. R. Tutty and T. J. Pedley, "Oscillatory flow in a stepped channel," *J. Fluid Mech.*, vol. 247, pp. 179–204, 1993.

[20] K. Zhou and J. C. Doyle, *Essentials of Robust Control*. Upper Saddle River, NJ: Prentice-Hall, 1998.

Lubomir Baramov received the Ing. (M.Sc. equivalent) degree in technical cybernetics from the Department of Electrical Engineering, Czech Technical University, Prague, in 1986 and the Ph.D. degree in engineering from the Department of Engineering Science, Osaka University, Japan, in 1996.

He was an Assistant Professor with the Czech Technical University, a part-time researcher with the Institute of Information Theory and Automation of the Czech Academy of Sciences, and a Research Fellow with the University of Southampton, U.K. He also held a two-year Postdoctoral position with the University of Tokyo, Japan, which was supported by the Japan Society for the Promotion of Science. Since 2001, he has been a Senior Research Engineer with Honeywell Prague Laboratory. His research interests include predictive, robust, and nonlinear control and control of fluid flows.

Owen Tutty received the B.Sc. and M.Sc. degrees in mathematics and applied mathematics from the University of Otago, New Zealand, and the Ph.D. degree in applied mathematics from Imperial College, U.K.

He was a Research Scientist with British Gas and a Research Associate with the Department of Applied Mathematics and Theoretical Physics, University of Cambridge, U.K. He has been with the University of Southampton, U.K., since 1986 where he is currently a Professor of Fluid Mechanics in the School of Engineering Sciences. His research interests span various areas of fundamental and computational fluid mechanics and flow control.

Eric Rogers received the B.Sc. degree in mechanical engineering from Queen's University, Belfast, U.K., and the M.Eng. and Ph.D. degrees in control systems and control theory, respectively, from The University of Sheffield, U.K.

He was a Lecturer in Mechanical Engineering with the University of Strathclyde, U.K. He has been with the University of Southampton, U.K., since 1990 where he is currently a Professor of Control Systems Theory and Design with the Department of Electronics and Computer Science. His major research interests are in multidimensional systems theory, with particular emphasis on the behavioral approach and systems with repetitive dynamics, the theory and application of iterative learning control, satellite control with particular emphasis on the suppression of micovibrations, and formation flying control, and flow control.

Dr. Rogers is the Editor of *The International Journal of Control* and an Associate Editor of *Multidimensional Systems and Signal Processing*.